





Hosohedral nodal-line superconductivity in hexagonal ABC Dirac semimetals

Hong-Guk Min ¹, Churlhi Lyi ¹, Moon Jip Park ^{2,3}✉ & Youngkuk Kim ¹✉

The recently identified hexagonal non-polar phase of KZnBi, an archetypal topological semimetal, has been found to cohost superconductivity on the surface. We propose that KZnBi can realize an unconventional topological superconductor featuring the hosohedral formation of nodal lines and Bogoliubov Fermi surface emerging under a magnetic field. Our density functional theory (DFT)-based low-energy model shows that the nonsymmorphic band degeneracy of the Dirac bands generically triggers topological nodal line superconductivity fostered by inter-band Coulomb interaction. In particular, the nodal lines of the gap resemble a hexagonal hosohedron with the Schläfli symbol of $\{2, 6\}$. Remarkably, the holohedral nodal line superconductor defines the topological phase boundary of the Bogoliubov Fermi surface in the limit where time-reversal symmetry is restored. Our results demonstrate that line nodes readily inflate to the Bogoliubov Fermi surface under an external magnetic field. We provide an experimentally verifiable explanation for the observed superconductivity and suggest a feasible platform for observing topological superconductivity in the hexagonal ABC ternary systems class.

¹Department of Physics, Sungkyunkwan University, Suwon 16419, Republic of Korea. ²Department of Physics, Hanyang University, Seoul 04763, Republic of Korea. ³Center for Theoretical Physics of Complex Systems, Institute for Basic Science (IBS), Daejeon 34126, Republic of Korea. ✉email: moonjippark@hanyang.ac.kr; youngkuk@skku.edu

Realization of topological superconductivity in a controllable platform holds a promise for the potential applications in quantum information science^{1–12}. Diverse Majorana platforms have been suggested, ranging from archetypal approaches that utilize topological superconductors^{13–20} to more recent approaches that benefit the proximity of superconductivity in heterostructures^{21–23}. These platforms have yielded convincing experimental evidence of the Majorana states^{24–32}. Nonetheless, searching for more scalable and controllable platforms is a pressing need for future developments. Encouragingly, routes to topological superconductivity are diversified, including more exotic classes that harbor gapless excitations such as the nodal plane Bogoliubov Fermi surface (BFS) superconductor^{33,34}.

The pioneering idea of proximity effect-induced superconductivity of topological surface states^{17,21} has subsequently generalized to simpler devices in wider varieties. For example, a doped topological insulator or a topological semimetal facilitates a single-material setting by driving bulk superconductivity^{35–37} with the advantage of the intrinsic surface and interband superconducting coherence in the momentum space. Conversely, known superconductors have been identified as topologically nontrivial^{38–40}. Furthermore, opportunities have been dilated beyond topological surface states, including the Shockley normal states⁴¹ with strong Rashba splitting, which drives Majorana zero modes under an external magnetic field^{42–44}.

A more exotic realization is a recently discovered surface superconductor that coexists with the bulk Dirac semimetal^{45–47}. A hexagonal nonpolar layered material KZnBi is a paradigmatic example whose bulk state hosts a topological Dirac semimetal in three dimensions. The onset of superconductivity is driven on the surface of KZnBi at $T_c = 0.85$ K⁴⁵. This peculiar situation provides a unique platform for intrinsic superconductivity of the three-dimensional massless Dirac fermions, dominated by the surface superconducting condensation. However, the character of the bulk superconducting state in this class of materials has remained unexplored.

In this Letter, we present a density functional theory (DFT)-based low-energy model that sheds light on the possible superconducting states of KZnBi. Our theory proposes a general scenario in which the nonsymmorphic band degeneracy of Dirac semimetals leads to stable nodal line superconductivity fostered by multiband interactions. To complement the experimental observations in KZnBi, we explicitly calculate the quasiparticle density of states and specific heat, which are in excellent agreement with the observed results. In particular, the nodal lines form a hexagonal hosohedron, which easily inflates to the BFS superconductors when time-reversal symmetry is broken, as we demonstrate by applying an external magnetic field. Our results suggest the emergence of an unconventional topological superconductor in KZnBi, offering a feasible route to finding smoking gun evidence of the Bogoliubov Fermi surface in the existing topological Dirac semimetal KZnBi.

Results and discussion

HNL superconductor in KZnBi. The present numerical study shows that KZnBi hosts a nodal superconductor with the hexagonal hosohedron formation of the nodal lines shown in Fig. 1b, which we refer to as the hosohedral nodal line (HNL) superconductor. The hosohedron refers to a geometric structure in which the tessellation of lunes on a spherical surface forms, such that each lune shares the same two polar opposite vertices. Fig. 1a delineates examples of the n -gonal hosohedrons ($n = 3, 4$, and 6), represented by the schläfli symbol $\{2, n\}$. A characteristic of the HNL superconductor is the superconducting gap highly suppressed near the polar vertices. More remarkably, the HNL

superconductor features the phase boundary of the BFS superconductors induced by time-reversal breaking perturbations, such as a magnetic field. Fig. 1b exemplifies the phase boundary of the BFS at zero magnetic fields. In the presence of the TR-breaking magnetic field, the HNL is immediately inflated to the BFS. We demonstrate this process in the KZnBi system.

KZnBi in hexagonal ABC crystals. We first clarify the crystalline symmetries of KZnBi. Fig. 2a shows the atomic structure of KZnBi as the representative case of the hexagonal non-polar ABC family. The unit cell comprises two formula units with six atoms (2Zn, 2Bi, 2K atoms). A layered structure is formed with two K layers (A-sublattice), which are intercalated by the two additional Zn-Bi layers with alternating Zn-Bi positions. The crystal structure preserves the symmetries of the non-symmorphic and centrosymmetric space group $P6_3/mmc$ (# 194), generated by inversion \mathcal{P} , sixfold screw $S_{6z} = \{C_{6z}|00\frac{1}{2}\}$, and two-fold rotation C_{2x} operations. Important symmetries include two mirrors m_z and a mirror m_x , protecting the Dirac crossings in the normal states bands with time-reversal symmetry \mathcal{T} . Similarly, the inversion \mathcal{P} and glide mirror $G_y = \{m_y|00\frac{1}{2}\}$ play a crucial role in protecting the nodal line superconducting phase.

Dirac semimetal in KZnBi. In good agreement with the previous study in Ref. 45, our density functional theory (DFT) calculations reproduce the Dirac bands. Fig. 2c shows the calculated DFT bands along the high-symmetry momenta shown in Fig. 2b. The magnified view of the band crossing in the inset clearly shows that a linear band crossing, referred to as the Dirac point (DP), appears along the high-symmetry Γ -A line in otherwise all gapped momentum space. Our calculation further reveals that the irreducible representations of the conduction and valence Dirac bands at A correspond to the A_6 and $A_4 \oplus A_5$ representations, respectively as indicated in Fig. 2c. The fourfold degeneracy at A is enforced by the m_x and \mathcal{PT} symmetries (See Supplementary Note 1 for the detailed symmetry analysis).

We construct a $\mathbf{k} \cdot \mathbf{p}$ minimal Hamiltonian that faithfully distills the Dirac bands of KZnBi. We propose the minimal eight-band model to capture the nonsymmorphic band degeneracy. The model Hamiltonian $\mathcal{H}_A(\mathbf{k})$ harbors the two four-fold degenerate states at $A_4 \oplus A_5$ and A_6 , such that it respects the symmetry constraints of the little group of A

$$\mathcal{H}_A(\mathbf{k}) = g\mathcal{H}(D_g^{-1}\mathbf{k})g^{-1}. \quad (1)$$

Here D_g is a symmetry operator defined in the momentum space, and g is the corresponding symmetry operator acting on the Bloch wave functions. The symmetry operators, g , are explicitly represented by $\mathcal{P} = -\sigma_x$, $C_{2x} = i(-\frac{\sqrt{3}}{2}s_x + \frac{1}{2}s_y)\tau_+ - is_z\tau_-$, $S_{6z} = -i\frac{\sqrt{3}}{2}s_z\tau_+\sigma_z - \frac{1}{2}\tau_-\sigma_z + \frac{1}{2}\tau_z\sigma_z$, and $\mathcal{T} = is_y\mathcal{K}$. Here, $\tau_{\pm} = (1 \pm \tau_z)/2$ and $\tau_z = \pm 1$ ($\sigma_z = \pm 1$) denote A_6 and $A_4 \oplus A_5$ (A_6^{\pm}) states, respectively. Similarly, $s_z = \pm 1$ describes spin, and \mathcal{K} is the complex conjugation. The detailed derivation of our model Hamiltonian is in Supplementary Note 1. In result, the explicit form of \mathcal{H}_A is given as follows;

$$\begin{aligned} \mathcal{H}_A = & m_k^+ \tau_+ + m_k^- \tau_- + \mu k_1 (k_1^2 - 3k_2^2) \sigma_y \\ & + \lambda_1 \left[k_1 (s_y + s_z) \tau_y + k_2 (\tau_x + s_x \tau_y) \right] \sigma_y \\ & + \lambda_2 k_z \left[l_1 s_x \tau_- + l_2 s_y \tau_- + l_3 s_z \tau_+ \right] \sigma_z \\ & + \lambda_3 \left[(k_1^2 - k_2^2) (\tau_x - s_x \tau_y) + 2k_1 k_2 (s_z \tau_y - s_y \tau_x) \right], \end{aligned} \quad (2)$$

$k_1 \equiv \frac{1}{2}k_x + \frac{\sqrt{3}}{2}k_y$, $k_2 \equiv \frac{\sqrt{3}}{2}k_x - \frac{1}{2}k_y$, and $m_k^{\pm} \equiv m_0^{\pm} + m_{\parallel}^{\pm} (k_1^2 + k_2^2) + m_z^{\pm} k_z^2$. The parameters m_0^{\pm} , m_{\parallel}^{\pm} , m_z^{\pm} , λ_i , μ , and l_i ($i = 1, 2, 3$)

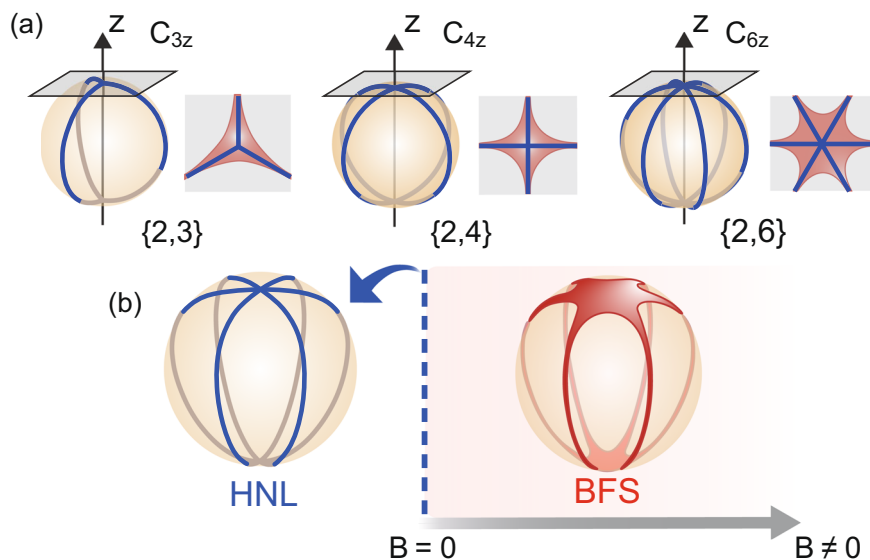


Fig. 1 Schematic figure of the hosohedral nodal lines (HNLs) and the Bogoliubov Fermi surface (BFS). **a** Illustration of C_n -symmetric n -gonal HNLs with the Schläfli symbol of $\{2, n\}$ for $n = 3, 4, 6$. The blue lines and orange spheroidal surfaces delineate the nodal lines and the Fermi surface, respectively. The top view of the nodal lines near the polar vertex of the hosohedron is shown with the nodal lines (blue) and the corresponding inflated BFS (red surface) in the gray plane. **b** Phase diagram in magnetic field B space. The HNL superconductors occur at the $B = 0$ phase boundary of the BFS superconductors, represented by a blue dashed line. The red surface illustrates BFS.

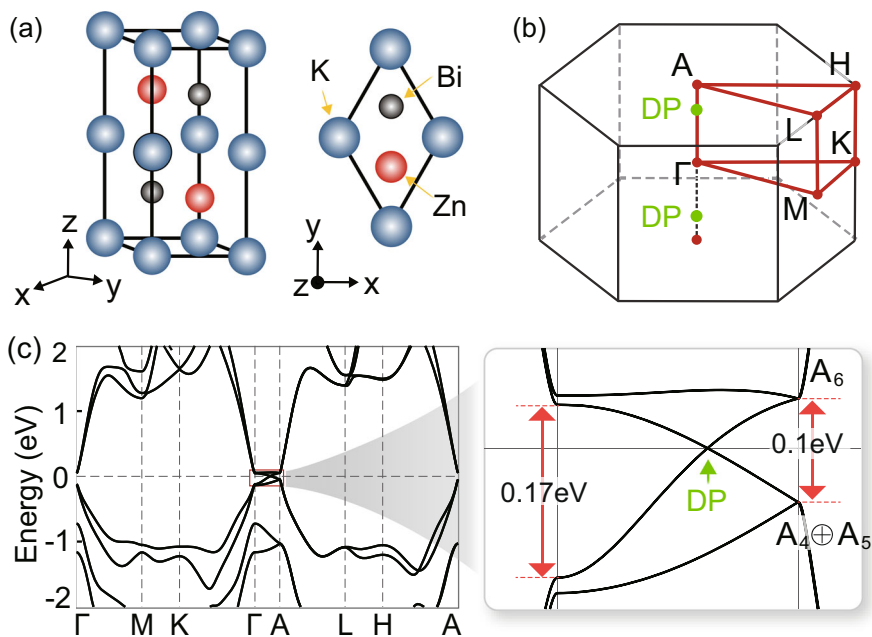


Fig. 2 Atomic and electronic structures of KZnBi. **a** Crystal structure of KZnBi. The solid black lines show the primitive unit cell. **b** Brillouin zone (BZ). High-symmetry momenta are colored red. Green solid circles indicate the position of the Dirac points (DPs). **c** Density functional theory (DFT) band structure of KZnBi. The inset shows the magnified view of the band crossing in the boxed region. The irreducible representations at the high-symmetry A point are provided, which are obtained for the DFT calculations.

are determined to reproduce the DFT bands of KZnBi near the Fermi energy (See Supplementary Note 1 for the full Hamiltonian and the parameters that reproduce the DFT bands of KZnBi).

Superconducting phases. We determine the possible pairings of the hole-doped bulk KZnBi superconductor, observed at $E_F = -50$ meV⁴⁵. We first classify the pairing functions based on the symmetries of D_{6h} , which admits the total twenty-eight distinct superconducting channels. The complete list of twenty-eight pairing functions can be found in Supplementary Note 2. Out of

these, three stable superconducting phases are found when the density-density type interactions are considered,

$$\mathcal{H}_1 = U \sum_i n_i^2 + 2V \sum_{i \neq j} n_i n_j, \quad (3)$$

where U (V) represents the intra-(inter-)band interaction strength, and $n_{i(j)}$ is a density operator for the electrons in the $i(j)$ -th orbital. (See Table 1 for the specific irreps and the corresponding gap structure).

Fig. 3a shows an exemplary phase diagram comprising stable channels for given sets of relative interaction strengths between V and U and the spin-orbit couplings λ_1 in a unit of the hopping parameter (m_{\parallel}^+). It is readily manifested from the phase diagram that $U < 0$ ($V < 0$) enhances the stability of Δ_{A1g} (Δ_{B2g} and Δ_{B2u}) phases. Furthermore, when the strong inter-band interaction regime, a strong SOC ($\lambda_1/m_{\parallel}^+ > 0.364 [a^{-1}]$) induces the HNL superconducting phase (Δ_{B2g}). The $\mathbf{k} \cdot \mathbf{p}$ parameters that reproduce the DFT bands satisfy the strong SOC criterion with $\lambda_1/m_{\parallel}^+ \sim 0.577 [a^{-1}]$, supporting the HNL phase in KZnBi.

Fig. 3b shows the calculated energy spectra for Δ_{B2g} , where the nodal lines are captured by the gap closing on the high-symmetry $A-\Gamma$ line. Since each branch is doubly degenerate, enforced by the $\mathcal{P}\mathcal{T}$ symmetry, the band crossings give rise to four-fold degeneracy. A close inspection of the zero nodes in the entire BZ leads to the hexagonal HNLs, where the nodal loop resides on the G_y invariant planes, including $k_y = 0$ and their C_{3z} -related planes (Fig. 3c).

Stability of the HNL. The symmetry analysis reveals that the glide mirror G_y plays a crucial role in stabilizing the four-fold

degeneracy of the HNL phase. To see this, we define the unitary chiral symmetry $\tilde{\chi} = i\tilde{T}\tilde{C}$ where $\tilde{\chi}^2 = 1$. The following mutual commutation relation holds between the symmetry operators of $\tilde{G}_y = G_y \oplus -G_y$, $\tilde{\chi}$ and the Bogoliubov-de Gennes (BdG) Hamiltonian \mathcal{H}_{BdG} of Δ_{B2g} phase (See Supplementary Note 2 for the detailed construction of the BdG Hamiltonian),

$$\begin{aligned} \{\tilde{\mathcal{P}}\tilde{T}, \tilde{G}_y\} &= 0, \{\tilde{\chi}, \tilde{G}_y\} = 0, \\ [\tilde{\mathcal{P}}\tilde{T}, \mathcal{H}_{\text{BdG}}] &= 0, \{\tilde{\chi}, \mathcal{H}_{\text{BdG}}\} = 0. \end{aligned} \quad (4)$$

For a given zero-energy eigenstate $|\psi_{E=0}\rangle$ with $\tilde{G}_y|\psi_{E=0}\rangle = |\psi_{E=0}\rangle$, the symmetry relations Eq. (4) ensure four mutually independent zero-energy states $\{|\psi_{E=0}\rangle, \tilde{\chi}|\psi_{E=0}\rangle, \tilde{\mathcal{P}}\tilde{T}|\psi_{E=0}\rangle, \tilde{\mathcal{P}}\tilde{T}\tilde{\chi}|\psi_{E=0}\rangle\}$. Thus, the presence of four-fold degeneracy at $E=0$ is compatible with the symmetries. The proof of mutual independence of these zero modes is given in Supplementary Note 2.

The HNL is topologically stable, protected by a non-zero topological $2\mathbb{Z}$ winding number. One-parameter families of inversion, time-reversal, and chiral symmetric superconductors (DIII+ \mathcal{P} class) can be characterized by a $2\mathbb{Z}$ winding number $\mathcal{N}_{\text{ID}}^{48,49}$

$$\mathcal{N}_{\text{ID}} = \frac{1}{2\pi i} \log \left(P \exp \oint_C d\mathbf{k} \cdot \nabla_{\mathbf{k}} \text{Tr} [\ln Q_{\mathbf{k}}] \right), \quad (5)$$

where P represents the path-ordering operator and $Q_{\mathbf{k}}$ is a unitary matrix obtained by flattening the positive energy spectrum of the BdG Hamiltonian (See Supplementary Note 2 for the precise definition of the $Q_{\mathbf{k}}$ matrices). Any path C that encloses a nodal line an odd number of times, as shown in Fig. 3c, generates the non-trivial winding number $\mathcal{N}_{\text{ID}} = 2$, which topologically

Δ	Interaction	Node	Irrep.
$S_x\sigma_y - S_x\tau_z\sigma_y$	V	Point	B_{2u}
S_y	U	Fully gapped	A_{1g}
$S_y\tau_z\sigma_x$	V	Line	B_{2g}

Representative pairing functions and their dependence on the interaction are listed in the first and second columns, respectively. (See Supplementary Table 2 for the full list of the pairing functions.) The gap structure is listed in the third column. The last column shows the corresponding irreducible representation (Irrep.) of the point group D_{6h} .

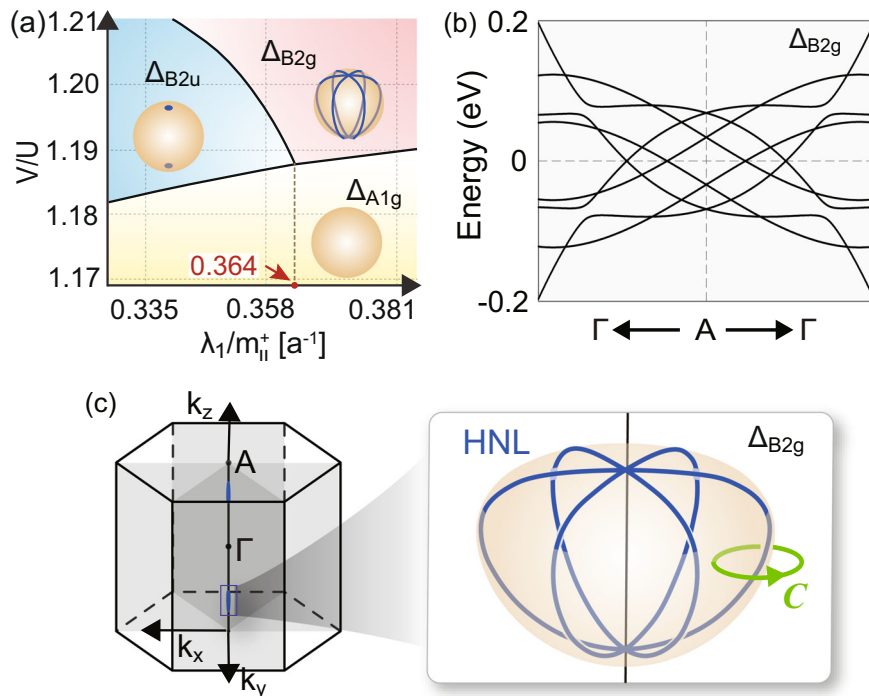


Fig. 3 Hosohedral nodal line (HNL) superconductor in Δ_{B2g} Pairing. **a** Phase diagram of the bulk superconducting phases of KZnBi. The phase diagram is calculated in terms of the V/U and $\lambda_1/m_{\parallel}^+$ parameter space, where V , U , λ_1 , and m_{\parallel}^+ are the inter-band Coulomb interaction, intra-band Coulomb interaction, spin-orbit coupling (SOC), and hopping parameters, respectively. Here, V/U is unitless, and $\lambda_1/m_{\parallel}^+$ is represented in units of the inverse lattice parameter a^{-1} . The Δ_{A2u} , Δ_{A1g} , and Δ_{B2g} orders dominate the blue, yellow, and red regions, respectively. **b** Bogolon quasiparticle energy spectra along the high-symmetry Γ - A - Γ line for the pairing functions Δ_{B2g} . **c** Nodal lines of Δ_{B2g} in the Brillouin zone. The winding number is calculated along the path C delineated by the green circle. The light orange surfaces represent the Fermi surfaces of the normal state.

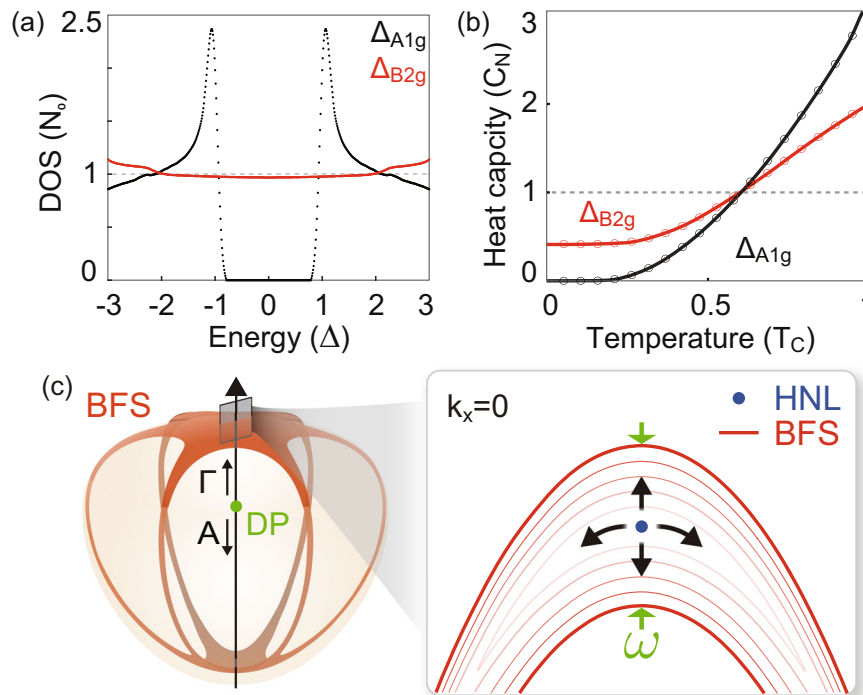


Fig. 4 Unique characteristics of the hosohedral nodal line (HNL) superconductor. **a** Density of the quasiparticle states N in the unit of the density of the normal states N_0 . **b** Temperature-divided specific heat of the superconducting state (C_s/T), normalized with the specific heat of the normal state at the critical temperature (C_n/T_c). Red (black) Dots represent the data points for Δ_{B2g} (Δ_{A1g}). The line plot of the same color was generated by interpolating the data points. **c** Inflation of an HNL to Bogoliubov Fermi surface (BFS) in momentum space. The green point and the light orange surface indicate the normal state Dirac point (DP) and the Fermi surface, respectively. The grey-boxed section is magnified in the right inset, which shows the cross-sectional view of the BFS in the $k_x = 0$ plane. The blue dot represents the intersecting point of the HNL penetrating the $k_x = 0$ plane. The red lines illustrate the inflated BFS. The ω marked with the green arrows indicates the size of inflation along the k_z axis.

protects the nodal lines. While $\mathcal{N}_{1D} = 2$ explains the stability of HNLs, hosting surface zero modes associated with the winding number may be improbable due to the general breaking of spatial inversion symmetry on the surface.

HNL state in KZnBi. The observed residual specific heat of KZnBi can be explained by the contributions of the finite density of states at the HNL phase⁴⁵. Our calculations show that the order parameter $|\Delta_{B2g}| \sim 10^{-1}$ meV order leads to the largest superconducting gap on the spheroidal surface of 0.04 meV. Fig. 4a shows the calculated DOS, which clearly shows that in stark contrast to the fully gapped superconducting state, the HNL phase exhibits a finite number of states. We also explicitly calculate the corresponding superconducting specific heat C_s in Fig. 4b as a function of normalized temperature T/T_c , where C_s is calculated by⁵⁰

$$C_s(T, \Delta) = \frac{1}{T} \sum_n \sum_k \left(E_{nk}^2 + \beta E_{nk} \frac{\partial \Delta}{\partial \beta} \frac{\partial E_{nk}}{\partial \Delta} \right) \left[- \frac{\partial f(E_{nk})}{\partial E_{nk}} \right], \quad (6)$$

where $\beta = \frac{1}{k_B T}$, k_B is the Boltzmann constant, and E_{nk} is the n -th quasiparticle energy at momentum \mathbf{k} . Near zero temperature, the C_s/T curve vanishes for the Δ_{A1g} pairing, while finite residual specific heat persists for the Δ_{B2g} pairing. The experiment⁴⁵ shows that the linear C_s/T versus T^2 plot yields a non-zero value near $T = 0$ K, which implies that the constant Fermionic contribution exists to the heat capacity even at the low temperature $T < 0.8$ K.

B-field induced BFS. We demonstrate that the HNL phase corresponds to the topological boundary of the BFS superconducting phase. Consequently, the magnetic field response of KZnBi offers

further definitive experimental evidence for the HNL phase through the inflation of HNLs into BFS. To demonstrate this, we introduce the additional Zeeman term $\mathcal{H}_{\text{Zeeman}} = -\mathbf{B} \cdot \boldsymbol{\mu}$ in the original Hamiltonian \mathcal{H}_A (Eq. (2)), where $\mathbf{B} = (B_x, B_y, B_z)$ is the magnetic field, and $\boldsymbol{\mu} = -g\mu_B \boldsymbol{\alpha}/\hbar$ is the magnetic moment. Here, the $\boldsymbol{\alpha} = (\alpha_x, \alpha_y, \alpha_z)$ is given by $\alpha_x = s_x(\tau_0 + \tau_z)/2$, $\alpha_y = -s_y(\tau_0 + \tau_z)/2$, and $\alpha_z = -s_z$, where μ_B is the Bohr magneton and g is the Landé g -factor, which can effectively account for the spin and orbital effects⁵¹. We set the $g = 2$ and $\hbar = 1$ for simplicity. The detailed derivation of the Zeeman Hamiltonian is in Supplementary Note 3. Fig. 4c shows the superconducting nodal surface calculated from the BdG Hamiltonian for $\Delta = \Delta_{B2g}$ in the presence of the z -directed magnetic field strength of $B_z = 0.5 \times 10^{-5}$ eV/ μ_B . We judiciously chose a minimal magnetic field value to demonstrate that BFS inflation occurs immediately upon applying the magnetic field. (See Supplementary Note 3 for the superconducting energy spectra calculated at larger B -fields). The nodes occur on a surface resembling the HNL shape.

We explicitly demonstrate the inflation of the nodal line into a BFS by directly calculating the evolution of the nodal structure as a function of an applied magnetic field. Fig. 4c shows the change of the nodal line at $k_x = 0$ plane as we increase the z -directed magnetic field strength B . We focus on the nodal structure near the upper polar vertices. The magnified view shows the intersection position between the nodal line and the $k_x = 0$ plane (solid blue dot), which occurs without a magnetic field. The red-colored lines show the cross-sectional position of the inflated BFS on the $k_x = 0$ plane that we obtain as we increase the magnetic field strength from zero to 0.5×10^{-5} eV/ μ_B . The zero-dimensional point inflates to one-dimensional lines, which demonstrates the inflation of the one-dimensional nodal lines

to the two-dimensional BFS. The size of inflation along the k_z axis (ω) is indicated by green arrows in Fig. 4c. The inflation width along the polar axis at the upper polar vertice ω is given by (See Supplementary Note 3 for the derivation.)

$$\omega = 2 \frac{g\mu_B B_z}{\hbar v_F}, \quad (7)$$

where v_F is the Fermi velocity along the out-of-plane z -direction. The layered geometry of KZnBi suppresses v_F into $0.61 \times 10^6 \text{ m s}^{-1}$, which is ten times weaker than the in-plane direction. Correspondingly, the BFS should be more prominent and observable in KZnBi.

Topological characterization of BFS. To further demonstrate the presence and stability of the BFS, we calculate the topological invariant associated with the nodal surface. The TR-broken superconductor with particle-hole symmetry belongs to the D symmetry class. In the three-dimensional momentum space, the nodal surfaces of the D class are protected by the \mathbb{Z}_2 invariant defined by a Pfaffian of the anti-symmetrized BdG Hamiltonian³³. Topological stability is attained when the Pfaffian at the nodal surface is zero, while the Pfaffian in momentum space separated by the nodal surface has a different sign. Accordingly, our calculations result in the negative (positive) sign of the Pfaffian in the interior (exterior) of the nodal surface. (See Supplementary Note 3 for the detailed calculation). Therefore, our explicit calculation demonstrates the magnetic field induces the topological BFS in the HNL superconducting. Thus, the observation of the BFS may be allowed in KZnBi under the magnetic field.

More ABC compounds. Our first-principles calculations predict more materials should realize the HNL superconductor from the family of ABC ternary compounds. Encouragingly, we have tested known non-polar hexagonal ABC materials obtained from the inorganic crystal structure database⁵² and found eight and four compounds from the I-XII-V and I-II-V groups that harbor the $\mathbf{k} \cdot \mathbf{p}$ effective model. The complete list of the candidate compounds is given in Supplementary Note 4. For example, the AZnBi ($A = \text{Na}$ and Li) and KMgBi are found to be a Dirac semimetal from I-XII-V and I-II-V groups, respectively. Moreover, $\text{NaZnBi}_{(1-x)}\text{Sb}_x$ should provide a tunable platform for engineering the band gap and topological properties as in the case of $\text{NaZnSb}_{(1-x)}\text{Bi}_x$ in a tetragonal phase⁵³.

Conclusion

In summary, we have studied the HNL superconducting phase in hexagonal ABC compounds based on the mean-field calculation using the $\mathbf{k} \cdot \mathbf{p}$ Hamiltonian. We find that the BFS can be achieved from the HNLs, by applying a time-reversal symmetry-breaking magnetic field. Furthermore, we attribute the microscopic mechanism of the superconductivity observed in Dirac semimetal KZnBi to the HNL superconductor. In this regard, the recent discovery of topological Dirac semimetal in KZnBi should provide an exciting opportunity for further study⁴⁵. Our theoretical prediction applies to the family of hexagonal ABC compounds, providing a catalog of candidate materials to realize the BFS.

Methods

Density functional theory calculations. The first-principles calculations based on the density functional theory were performed using the VASP package⁵⁴. The modified Becke-Johnson (mBJ) meta-generalized gradient approximation (GGA)⁵⁵ was used to describe the exchange-correlation energy, with the corresponding mBJ parameter $\text{CMBJ} = 1.2865$. The non-collinear spin-orbit coupling was included, and the plane-wave energy cutoff of 278 eV was

given throughout the calculations. The lattice constants of KZnBi were set to be $a = 4.68 \text{ \AA}$ and $c = 10.65 \text{ \AA}$, adapting the results of the previous work⁴⁵. The self-consistent charge density was obtained on a uniformly sampled $12 \times 12 \times 4$ momentum grid, and the total energy successfully converged below 10^{-7} eV criterion.

Mean-field calculations. To calculate the superconducting phase diagram, we first fixed the hopping parameter m_{\parallel}^+ and varied the SOC parameter λ_1 . For a given λ_1 , we determined the intra-band interaction strength U that yields $|\Delta_{\text{A1g}}| = 5 \text{ meV}$. This strength ranged from -4.93 eV to -5.32 eV . With this fixed value of U as a reference, we varied the magnitude of the inter-band interaction V and solved the gap equation to identify the energetically favored gap function. To solve the multi-band gap equation and determine the magnitude of the superconducting order parameter, we used the methods described by Kim et al.⁵⁶.

Data availability

The authors ensure the availability of the data supporting the findings of the current study in both the article and its Supplementary Materials. Additional information can be provided upon request.

Received: 24 April 2023; Accepted: 11 December 2023;

Published online: 05 January 2024

References

- Majorana, E. Teoria simmetrica dell'elettrone e del positrone. *Nuovo Cim.* **14**, 171 (1937).
- Wilczek, F. Majorana returns. *Nat. Phys.* **5**, 614 (2009).
- Kitaev, A. Y. Fault-tolerant quantum computation by anyons. *Ann. Phys.* **303**, 2 (2003).
- Nayak, C., Simon, S. H., Stern, A., Freedman, M. & Sarma, S. D. Non-Abelian anyons and topological quantum computation. *Rev. Mod. Phys.* **80**, 1083 (2008).
- Qi, X.-L. & Zhang, S.-C. Topological insulators and superconductors. *Rev. Mod. Phys.* **83**, 1057 (2011).
- Alicea, J., Oreg, Y., Refael, G., Von Oppen, F. & Fisher, M. Non-Abelian statistics and topological quantum information processing in 1D wire networks. *Nature Physics* **7**, 412 (2011).
- Van Heck, B., Akhmerov, A., Hassler, F., Burrello, M. & Beenakker, C. Coulomb-assisted braiding of Majorana fermions in a Josephson junction array. *New J. Phys.* **14**, 035019 (2012).
- Douçot, B. & Ioffe, L. Physical implementation of protected qubits. *Rep. Prog. Phys.* **75**, 072001 (2012).
- Hyart, T. et al. Flux-controlled quantum computation with Majorana fermions. *Phys. Rev. B* **88**, 035121 (2013).
- Landau, L. et al. Towards realistic implementations of a majorana surface code. *Phys. Rev. Lett.* **116**, 050501 (2016).
- Aasen, D. et al. Milestones toward majorana-based quantum computing. *Phys. Rev. X* **6**, 031016 (2016).
- Gül, Ö. et al. Ballistic Majorana nanowire devices. *Nat. Nanotechnol.* **13**, 192 (2018).
- Volovik, G. Fermion zero modes on vortices in chiral superconductors. *J. Exp. Theor. Phys.* **70**, 609 (1999).
- Read, N. & Green, D. Paired states of fermions in two dimensions with breaking of parity and time-reversal symmetries and the fractional quantum Hall effect. *Phys. Rev. B* **61**, 10267 (2000).
- Ivanov, D. A. Non-abelian statistics of half-quantum vortices in p-wave superconductors. *Phys. Rev. Lett.* **86**, 268 (2001).
- Kitaev, A. Y. Unpaired Majorana fermions in quantum wires. *Phys.-Uspekhi* **44**, 131 (2001).
- Sato, M. Non-Abelian statistics of axion strings. *Phys. Lett. B* **575**, 126 (2003).
- Fu, L. & Berg, E. Odd-parity topological superconductors: theory and application to $\text{Cu}_x\text{Bi}_2\text{Se}_3$. *Phys. Rev. Lett.* **105**, 097001 (2010).
- Sasaki, S. et al. Topological superconductivity in $\text{Cu}_x\text{Bi}_2\text{Se}_3$. *Phys. Rev. Lett.* **107**, 217001 (2011).
- Levy, N. et al. Experimental evidence for s-wave pairing symmetry in superconducting $\text{Cu}_x\text{Bi}_2\text{Se}_3$ single crystals using a scanning tunneling microscope. *Phys. Rev. Lett.* **110**, 117001 (2013).

21. Fu, L. & Kane, C. L. Superconducting proximity effect and majorana fermions at the surface of a topological insulator. *Phys. Rev. Lett.* **100**, 096407 (2008).
22. Shabani, J. et al. Two-dimensional epitaxial superconductor-semiconductor heterostructures: A platform for topological superconducting networks. *Phys. Rev. B* **93**, 155402 (2016).
23. Frolov, S., Manfra, M. & Sau, J. Topological superconductivity in hybrid devices. *Nat. Phys.* **16**, 718 (2020).
24. Mourik, V. et al. Signatures of majorana fermions in hybrid superconductor-semiconductor nanowire devices. *Science* **336**, 1003 (2012).
25. Rokhinson, L. P., Liu, X. & Furdyna, J. K. The fractional a.c. Josephson effect in a semiconductor-superconductor nanowire as a signature of Majorana particles. *Nat. Phys.* **8**, 795 (2012).
26. Das, A. et al. Zero-bias peaks and splitting in an Al-InAs nanowire topological superconductor as a signature of Majorana fermions. *Nat. Phys.* **8**, 887 (2012).
27. Finck, A. D. K., Van Harlingen, D. J., Mohseni, P. K., Jung, K. & Li, X. Anomalous modulation of a zero-bias peak in a hybrid nanowire-superconductor device. *Phys. Rev. Lett.* **110**, 126406 (2013).
28. Churchill, H. O. H. et al. Superconductor-nanowire devices from tunneling to the multichannel regime: Zero-bias oscillations and magnetoconductance crossover. *Phys. Rev. B* **87**, 241401 (2013).
29. Nadj-Perge, S. et al. Observation of Majorana fermions in ferromagnetic atomic chains on a superconductor. *Science* **346**, 602 (2014).
30. Xu, S.-Y. et al. Momentum-space imaging of Cooper pairing in a half-Dirac-gas topological superconductor. *Nat. Phys.* **10**, 943 (2014).
31. Albrecht, S. M. et al. Exponential protection of zero modes in Majorana islands. *Nature* **531**, 206 (2016).
32. Deng, M. et al. Majorana bound state in a coupled quantum-dot hybrid-nanowire system. *Science* **354**, 1557 (2016).
33. Agterberg, D., Brydon, P. & Timm, C. Bogoliubov Fermi Surfaces in Superconductors with Broken Time-Reversal Symmetry. *Phys. Rev. Lett.* **118**, 127001 (2017).
34. Bzdušek, T. & Sigrist, M. Robust doubly charged nodal lines and nodal surfaces in centrosymmetric systems. *Phys. Rev. B* **96**, 155105 (2017).
35. Wang, Z. et al. Topological nature of the FeSe_{0.5}Te_{0.5} superconductor. *Phys. Rev. B* **92**, 115119 (2015).
36. Wu, X., Qin, S., Liang, Y., Fan, H. & Hu, J. Topological characters in Fe(Te_{1-x}Se_x) thin films. *Phys. Rev. B* **93**, 115129 (2016).
37. Zhang, P. et al. Observation of topological superconductivity on the surface of an iron-based superconductor. *Science* **360**, 182 (2018).
38. Yan, B., Jansen, M. & Felser, C. A large-energy-gap oxide topological insulator based on the superconductor BaBiO₃. *Nat. Phys.* **9**, 709 (2013).
39. Kim, M., Wang, C.-Z. & Ho, K.-M. Topological states in A15 superconductors. *Phys. Rev. B* **99**, 224506 (2019).
40. Zhao, N.-N. et al. Topological properties of Mo₂C and W₂C superconductors. *Phys. Rev. B* **101**, 195144 (2020).
41. Shockley, W. On the surface states associated with a periodic potential. *Phys. Rev.* **56**, 317 (1939).
42. Sato, M., Takahashi, Y. & Fujimoto, S. Non-abelian topological order in s-wave superfluids of ultracold fermionic atoms. *Phys. Rev. Lett.* **103**, 020401 (2009).
43. Lutchyn, R. M., Sau, J. D. & Sarma, S. D. Majorana fermions and a topological phase transition in semiconductor-superconductor heterostructures. *Phys. Rev. Lett.* **105**, 077001 (2010).
44. Oreg, Y., Refael, G. & von Oppen, F. Helical liquids and majorana bound states in quantum wires. *Phys. Rev. Lett.* **105**, 177002 (2010).
45. Song, J. et al. Coexistence of surface superconducting and three-dimensional topological dirac states in semimetal KZnBi. *Phys. Rev. X* **11**, 021065 (2021).
46. Liu, Q. et al. Observation of surface superconductivity in a 3D dirac material. *Adv. Funct. Mater.* **32**, 2208616 (2022).
47. Schwemmer, T., Di Sante, D., Schmalian, J. & Thomale, R. Chiral surface superconductivity in half-Heusler semimetals. arxiv:2212.09786, (2022).
48. Snyder, A. P., Ryu, S., Furusaki, A. & Ludwig, A. W. W. Classification of topological insulators and superconductors in three spatial dimensions. *Phys. Rev. B* **78**, 195125 (2008).
49. Bzdušek, T. & Sigrist, M. Robust doubly charged nodal lines and nodal surfaces in centrosymmetric systems. *Phys. Rev. B* **96**, 155105 (2017).
50. Hashimoto, T., Kobayashi, S., Tanaka, Y. & Sato, M. Superconductivity in doped Dirac semimetals. *Phys. Rev. B* **94**, 014510 (2016).
51. Lei, C., Chen, H. & MacDonald, A. H. Ultrathin films of superconducting metals as a platform for topological superconductivity. *Phys. Rev. Lett.* **121**, 227701 (2018).
52. Levin, I. Nist inorganic crystal structure database (icsd), <https://doi.org/10.18434/M32147> (2020).
53. Jeong, J., Kim, D. & Kim, Y. Topological phase transitions without symmetry indication in NaZnSb_{1-x}Bi_x. *Sci. Rep.* **12** <https://doi.org/10.1038/s41598-022-26596-y> (2022).
54. Kresse, G. & Furthmüller, J. Efficient iterative schemes for ab initio total-energy calculations using a plane-wave basis set. *Phys. Rev. B* **54**, 11169 (1996).
55. Tran, F. & Blaha, P. Accurate band gaps of semiconductors and insulators with a semilocal exchange-correlation potential. *Phys. Rev. Lett.* **102**, 226401 (2009).
56. Kim, Y., Hankiewicz, E. M. & Gilbert, M. J. Topological excitonic superfluids in three dimensions. *Phys. Rev. B* **86**, 184504 (2012).

Acknowledgements

This research was supported by the SungKyunKwan University and the BK21 FOUR (Graduate School Innovation) funded by the Ministry of Education (MOE, Korea) and National Research Foundation of Korea (NRF). Y.K. acknowledges the support from the National Research Foundation of Korea (NRF) (Grant No. NRF-2021R1A2C1013871). M.J.P. acknowledges the support from the NRF grant funded by the Korean government (MSIT) (Grants No. RS-2023-00252085 and No. RS-2023-00218998) and financial support from the Institute for Basic Science in the Republic of Korea through the project IBS-R024-D1. The computational resource is provided by the Korea Institute of Science and Technology Information (KISTI) (KSC-2021-CRE-0116).

Author contributions

H.G.M. developed the effective Hamiltonian and performed the mean-field calculations. C.L. performed ab initio calculations. H.G.M. and Y.K. constructed the manuscript. M.J.P. and Y.K. helped with the calculation and strengthened the discussion. All authors contributed to the manuscript.

Competing interests

The authors declare no competing interests.

Additional information

Supplementary information The online version contains supplementary material available at <https://doi.org/10.1038/s42005-023-01501-9>.

Correspondence and requests for materials should be addressed to Moon Jip Park or Youngkuk Kim.

Peer review information *Communications Physics* thanks Feng Liu and the other, anonymous, reviewer(s) for their contribution to the peer review of this work. A peer review file is available.

Reprints and permission information is available at <http://www.nature.com/reprints>

Publisher's note Springer Nature remains neutral with regard to jurisdictional claims in published maps and institutional affiliations.



Open Access This article is licensed under a Creative Commons Attribution 4.0 International License, which permits use, sharing, adaptation, distribution and reproduction in any medium or format, as long as you give appropriate credit to the original author(s) and the source, provide a link to the Creative Commons license, and indicate if changes were made. The images or other third party material in this article are included in the article's Creative Commons license, unless indicated otherwise in a credit line to the material. If material is not included in the article's Creative Commons license and your intended use is not permitted by statutory regulation or exceeds the permitted use, you will need to obtain permission directly from the copyright holder. To view a copy of this license, visit <http://creativecommons.org/licenses/by/4.0/>.

© The Author(s) 2024